PCCP

RSC Publishing

PAPER

View Article Online
View Journal | View Issue

Cite this: *Phys. Chem. Chem. Phys.*, 2013, **15**, 16152

High energy resolution core-level X-ray spectroscopy for electronic and structural characterization of osmium compounds

Kirill A. Lomachenko,[ab] Claudio Garino,*[a] Erik Gallo,[ac] Diego Gianolio,[d] Roberto Gobetto,[a] Pieter Glatzel,[c] Nikolay Smolentsev,[b] Grigory Smolentsev,[e] Alexander V. Soldatov,[b] Carlo Lamberti[a] and Luca Salassa[f]

Received 3rd May 2013,
Accepted 1st August 2013

DOI: 10.1039/c3cp51880a

www.rsc.org/pccp

A comprehensive study of the bulk solid $OsCl_3$ and the molecular ion $[Os(bpy)_2(CO)Cl]^+$ is presented illustrating the application of RIXS and HERFD XANES spectroscopies to the investigation of both bulk materials and molecular complexes. In order to analyze the experimental results, DFT simulations were performed taking into account spin–orbit interaction. Calculations for both compounds resulted in good agreement with the experimental RIXS and HERFD XANES data, shedding light on the details of their local atomic and electronic structure. In particular, the spatial distribution of molecular orbitals was obtained, which allowed the determination of the origin of the absorption peaks. It was shown that for materials containing heavy atoms, only the application of advanced RIXS and HERFD XANES spectroscopies makes it possible to extract the information on local atomic and electronic structure details from XANES data.

Introduction

Resonant inelastic X-ray scattering (RIXS), synonymously called in the literature resonant X-ray emission spectroscopy (RXES), has proven to be an effective tool for the determination of the local atomic and electronic structure of various chemical systems. This technique was successfully used for the study of bulk materials, nanoparticles and molecular metal complexes.[1–4] Being element-selective, RIXS provides specific information on both occupied and unoccupied orbitals with contributions from the probed atom (*e.g.* the metal ion in a metal complex). The two-photon RIXS process consists of the promotion of a core electron to an unoccupied orbital above the Fermi level as a result of the X-ray photon absorption and consequent filling of the core vacancy by one of the electrons from higher-lying energy levels, which is accompanied by the emission of a fluorescence photon.[5] Depending on the origin of this radiative transition, valence-to-core and core-to-core RIXS are distinguished. In the former, the core hole is filled by electrons from the valence band (or valence orbitals in case of molecular systems), which results in energy transfer of the order of several eV. This makes valence-to-core RIXS a tool to study electronic transitions similar to UV-Vis spectroscopy, although RIXS is sensitive to d–d transitions, while in UV-Vis such transitions are generally dipole forbidden and hence very weak. In the case of core-to-core RIXS, the vacancy is filled as a result of transitions from a core level with higher energy. Core-to-core RIXS data are invaluable for clear understanding of the origin of pre-edge features, analyzing multiplet effects, and obtaining high resolution absorption spectra. Experimentally, RIXS data are collected by scanning both the incident X-ray energy (Ω) by means of the monochromator, and the energy of emitted radiation (ω), employing the analyzer crystals. Resultant two-dimensional intensity distributions (RIXS maps) are plotted *versus* the incident energy and the energy transfer (*i.e.* $\Omega - \omega$). Tuning the analyzer crystals to select only those fluorescence photons whose energy corresponds to the maximum intensity of a particular emission line and scanning the incident energy results in the high energy resolution fluorescent detection X-ray absorption near edge structure (HERFD XANES) spectra.[6–8]

The resolution gain of HERFD XANES over standard total fluorescence yield (TFY) XANES is higher for the measurement of heavy elements such as rare-earth and 5d metals. In particular,

[a] *Department of Chemistry and NIS Centre of Excellence, University of Turin, Via P. Giuria 7, 10125 Turin, Italy. E-mail: claudio.garino@unito.it; Fax: +39 011 6707855; Tel: +39 011 6707943*
[b] *Research Center for Nanoscale Structure of Matter, Southern Federal University, ul. Zorge 5, 344090 Rostov-on-Don, Russia*
[c] *European Synchrotron Radiation Facility (ESRF), 6 Rue Jules Horowitz, 38043 Grenoble, France*
[d] *Diamond Light Source Ltd, Harwell Science and Innovation Campus, OX11 0DE Didcot, UK*
[e] *Paul Scherrer Institute, 5232 Villigen, Switzerland*
[f] *CIC biomaGUNE, Paseo Miramón 182, 20009 Donostia – San Sebastián, Spain*

the osmium $2p_{3/2}$ level has a width of 5.16 eV,[9] which makes the conventional L_3-edge spectra very broad, almost featureless and therefore hardly informative. As a result, there are very few studies which apply XANES to Os compounds. Most of them are carried out in the field of geochemistry, addressing almost exclusively the energy and intensity of the L_3-edge main peak,[10–13] the so-called white line.[8] Recent studies, in which osmium complexes are found to show very promising results as potential anticancer drugs and dyes for dye-sensitized solar cells employ mostly optical spectroscopy and X-ray diffraction techniques for characterization.[14–18] Here we illustrate the advantages of RIXS and HERFD XANES spectroscopies for the study of osmium compounds on the example of osmium trichloride, $OsCl_3$ (**1**) and bis(2,2′-bipyridine)carbonylchloroosmium(II) ion, $[Os(bpy)_2(CO)Cl]^+$ (**2**). Combined with DFT calculations, spectroscopic data serve as a probe for the quality of the calculated geometry and electronic structure of the compounds under study.

Materials and methods

Experimental section

Experimental HERFD XANES and TFY XANES spectra of Os L_3-edge in compounds **1** and **2** together with the corresponding RIXS maps were collected on the high brilliance X-ray spectroscopy beamline ID26 at the European Synchrotron Radiation Facility (ESRF). Recording the corresponding core-to-core RIXS maps prior to measuring high resolution XANES is always necessary in order to check the origin of new peaks which can appear in HERFD spectra and be absent in the standard TFY ones. If this initial control is not performed, spectral features can be erroneously assigned to the increase of the resolution, whereas in fact they might be the result of the off-diagonal multiplet states.[19]

Compound **1** was purchased from Sigma Aldrich and measured as powder, while complex **2** with a $[PF_6]^-$ counter ion was prepared as previously reported[20] and its measurements were carried out both in solid phase and in acetone solution. XANES spectra were obtained as an average of several consecutive scans, thus allowing the monitoring of radiation damage. Solution measurements were performed in thin capillaries, moved under the beam in order to prevent any possible radiation damage occurring under prolonged exposure. For both solid and solution RIXS measurements, the absence of damage was verified by the lack of changes in the XANES spectra measured before and after the map acquisition.

Core-to-core RIXS maps were measured around the Os $L\alpha_1$ emission line. High resolution XANES spectra were collected detecting only photons, whose energy corresponded to the maximum intensity of this emission line. For the incident radiation a flat double crystal Si (111) monochromator was used. Its energy resolution for osmium L_3 edge (10 871 eV) was 1.5 eV. As analyzer crystals, two Ge (100) (800 reflection) with 1.1 eV resolution were employed in vertical Rowland geometry. The crystals were spherically bent following the Johann scheme to focus fluorescent radiation on the APD detector. The current in the storage ring was about 200 mA, which resulted in a flux on the sample of around 5×10^{13} photons per second. The beam size on the sample was around 0.8 mm by 0.2 mm.

Theory

In order to refine the structure of the studied compounds, geometry optimization was performed by means of density functional theory (DFT). For (**1**), the periodic code BAND2012[21–23] was used together with the TZP basis set,[24] the scalar ZORA formalism[25–27] and the PBE functional.[28] For further calculation of XANES and RIXS, the Os_4Cl_{12} cluster was cut from the bulk structure. The optimization of the structure of **2** was carried out by the ADF2010 package[29–31] using the TZ2P basis set and the scalar ZORA approach. A set of popular GGA functionals including PBE, BLYP (Becke exchange[32] with LYP correlation[33]) and OPBE (OPTX exchange[34] with PBE correlation) was employed, as a reasonable compromise between the fast but not always accurate local density approximation[35] and the computationally demanding hybrid functionals. Ground state spin multiplicities of both compounds were set to 1. The nature of the stationary points was confirmed by the normal-mode analysis. The three above mentioned GGA functionals were used in XANES calculations for both compounds. One of the most popular hybrids, B3LYP,[33,36] was reported to provide poor results modeling the absorption spectra of similar systems with ADF2010[37] and therefore was not employed in the current work.

Depending on the strength of the multiplet effects in the system, the adequate theoretical treatment should be chosen. In the case of shallow 2p core levels of 3d transition metals, they are very pronounced and therefore cannot be neglected. Among the approaches to analyze these transitions is the charge transfer multiplet (CTM) method developed by de Groot *et al.*,[38,39] the *ab initio* CTM by Tanaka *et al.*,[40] and the configuration interaction (CI) schemes, namely by Haverkort *et al.*[41] and Bagus *et al.*[42] However, these methods either contain many empirical parameters or are very costly in terms of CPU time which generally limits their application to very small systems with high symmetry. A new DFT/ROCIS approach which combines the relatively high speed of DFT calculations and the accurate treatment of the multiplets possible with CI was presented recently by Neese's group.[43] The first results obtained for both molecules[44] and large solid state systems[45] were promising, but nonetheless it is evident that taking full account of the multiplet effects in $L_{2,3}$-edges of 3d transition metals is still a very challenging task. In the $L_{2,3}$-edges of 4d and, primarily, 5d metals, multiplet effects are known to be much less pronounced,[46] and can consequently be neglected in the first approximation. Therefore, a single-electron transition approximation generally yields good results when applied for such systems.[47,48]

Calculation of HERFD XANES spectra was performed using two different tools. The first was the well-established FDMNES code,[49,50] which solves the Schrödinger equation on a discrete grid of points by the finite difference method. The code uses the Hedin and Lundqvist exchange–correlation model and allows the calculations to be performed without any restrictions for the shape of the potential, which is often of particular importance for molecules and structures with cavities and channels.

The second approach was based on the molecular orbital data, computed by ADF as a result of all-electron single point calculations. Molecular orbitals of interest were projected onto the three-dimensional cubic grid centered on the absorbing atom. For the L_3 edge XANES, these were four $2p_{3/2}$ orbitals and several hundred unoccupied orbitals above the LUMO. The spectrum was formed as a result of the calculation of dipole matrix elements for transitions between the occupied and unoccupied orbitals:

$$I_{\mathrm{XAS\,L_3}} \sim \sum_{k=1}^{4} \sum_{j=\mathrm{LUMO}}^{\mathrm{LUMO+N}} \left| \left\langle f_j \middle| \hat{d} \middle| i_k \right\rangle \right|^2 \qquad (1)$$

where $\hat{d}$ is the dipole operator, i and f are core and unoccupied orbitals, respectively, k specifies four Os $2p_{3/2}$ orbitals and j runs over N unoccupied orbitals above the LUMO. N is typically of the order of several hundred, depending on the chosen basis set and the energy range to be calculated.

Numerical integration was performed by a separate in-house program.[51] The parameters of the grid are mainly defined by the distribution of core orbitals, since they are much more localized than the unoccupied ones and therefore determine the decay of the matrix element integral. For the osmium compounds under study, convergence was reached for the grid with the edge length of 0.5 Å and a linear density of 60 points per Ångström. These parameters were used for all the calculations presented. In both theoretical approaches the arctangent energy-dependent broadening was applied to the initially obtained discrete spectra in order to match the resolution of experimental data.

Single-point calculations were performed with already optimized structures. In the case of **1**, calculations using OPBE, BLYP and PBE were performed on the same geometry, whereas for **2** the functional employed for each single point calculation was the one adopted for geometry optimization of the corresponding structure. In order to take into account relativistic effects and spin–orbit interaction, the two-component ZORA approximation was applied.

Core-to-core RIXS maps were calculated using ADF molecular orbitals as input, similarly to HERFD XANES: numerical values of Os $2p_{3/2}$, $3d_{5/2}$ and unoccupied orbitals were projected on the cubic grid around the osmium atom and then L_3 XANES and $L\alpha_1$ XES spectra were calculated. For the latter, the following expression was used:

$$I_{\mathrm{XES\,L\alpha_1}} \sim \sum_{k=1}^{4} \sum_{j=1}^{6} \left| \left\langle f_k \middle| \hat{d} \middle| i_j \right\rangle \right|^2 \qquad (2)$$

where $\hat{d}$ is the dipole operator, and i and f are Os $3d_{5/2}$ and $2p_{3/2}$ orbitals respectively.

XANES and XES spectra for each of the $2p_{3/2}$ orbitals were then inserted in the formula[52] derived from the Krammers–Heisenberg equation[53,54] neglecting the interference and multiplet effects:

$$F(\Omega,\omega) = \sum_{k=1}^{4} \int_{\varepsilon} \frac{I_{k\,\mathrm{XES\,L\alpha_1}}(\varepsilon) I_{k\,\mathrm{XAS\,L_3}}(\varepsilon+\Omega-\omega)}{(\varepsilon-\omega)^2 + \frac{\Gamma_{2p}^2}{4}} \mathrm{d}\varepsilon \qquad (3)$$

Here Γ_{2p} is the lifetime broadening of the Os $2p_{3/2}$ level, Ω and ω are energies of incoming and fluorescent radiation respectively, k enumerates Os $2p_{3/2}$ orbitals.

Results and discussion

The structures of **1** and **2** are schematically depicted in Fig. 1, while the computed structural parameters are presented in Table 1. In total, four different geometries were obtained (one for compound **1** and three for complex **2**). For compound **1**, the first coordination shell of Os consists of six Cl atoms in the slightly distorted octahedral geometry, while the second shell is formed by three Os atoms. Complex **2** also contains a six-neighbored Os atom, although its nearest coordination is much more distorted, comprising four nitrogens as well as chloride and carbonyl ligands. Optimization using different functionals yields similar results and in most cases the optimized bond lengths are in agreement with the X-ray diffraction structure.[55] A systematic difference found is the increase of the C–H bond lengths from 0.93 Å (experimental) to 1.09 Å (calculation), which is not surprising since hydrogen positions are hard to extract from X-ray diffraction data. Complex **2** with triflate as a counter ion was reported by Croce *et al.*[56] and no significant structural differences from the complex with hexafluorophosphate were indicated. Due to this fact and taking into account the rather

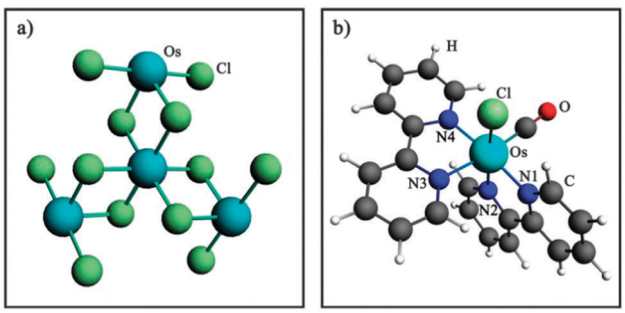

Fig. 1 Structures of $OsCl_3$ (a) and $[Os(bpy)_2(CO)Cl]^+$ (b) used for calculations of XANES. For the optimized distances of both structures see Table 1.

Table 1 Values of structural parameters for $OsCl_3$ and $[Os(bpy)_2(CO)Cl]^+$

$OsCl_3$	
Parameter	PBE
Os–Cl (Å)	2.38
Os–Os (Å)	3.39
$Cl–Os–Cl_{\parallel}$ (deg)	178.8
$Cl–Os–Cl_{\perp}$ (deg)	89.0–90.7

$[Os(bpy)_2(CO)Cl]^+$				
Parameter	XRD	OPBE	BLYP	PBE
Os–N1 (Å)	2.07	2.07	2.12	2.09
Os–N2 (Å)	2.08	2.06	2.12	2.08
Os–N3 (Å)	2.08	2.13	2.18	2.15
Os–N4 (Å)	2.07	2.03	2.08	2.05
Os–C (Å)	1.79	1.84	1.88	1.87
Os–Cl (Å)	2.32	2.35	2.42	2.39
C–H (Å)	0.93	1.09	1.09	1.09

large distance between the metal center and the counter ion, we did not include the latter in the structure optimization and XANES and RIXS simulation.

The experimental Os $L\alpha_1$ RIXS maps of the two compounds are reported in the top part of Fig. 2. The absence of non-diagonal peaks on the RIXS maps suggests a relatively small role of multiplet effects in the absorption process for these 5d-metal systems, justifying the choice of single-electron transition approximation for theoretical modeling of RIXS maps and HERFD XANES spectra. The simulated RIXS maps for both compounds under study are shown in the bottom part of Fig. 2. The map for **1** was calculated using the electronic structure obtained with a BLYP functional, whereas for **2** the OPBE one was employed since these functionals showed the best performance in XANES simulations for the corresponding structures (*vide infra*). The theoretical maps exhibit a good qualitative agreement with the experiment, correctly reproducing the shape of the maxima.

An experimental HERFD XANES spectrum corresponds to a diagonal cut through the RIXS plane where the axes are incident photon energy and energy transfer.[57] The later is the difference between the energies of incident and emitted radiation ($\Omega - \omega$).

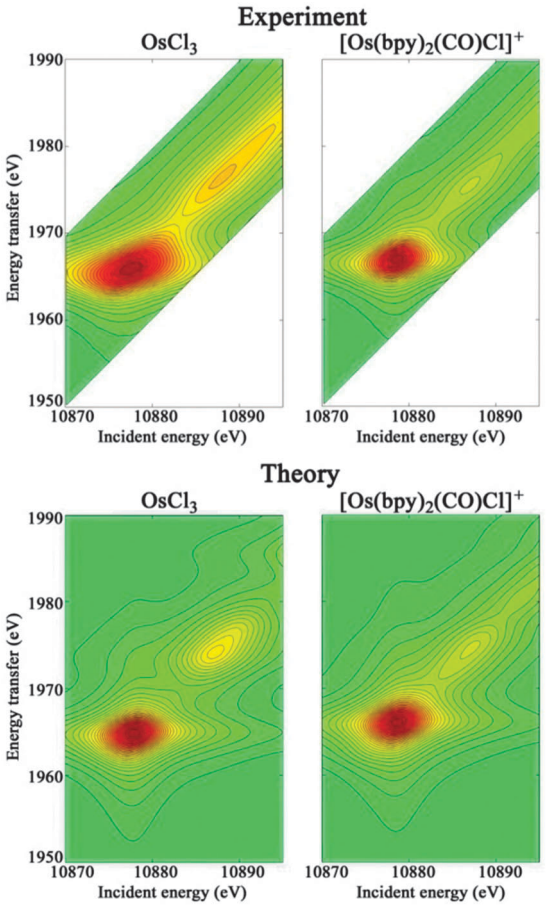

Fig. 2 Experimental (top) and simulated (bottom) $L\alpha_1$ RIXS maps of $OsCl_3$ and $[Os(bpy)_2(CO)Cl]^+$.

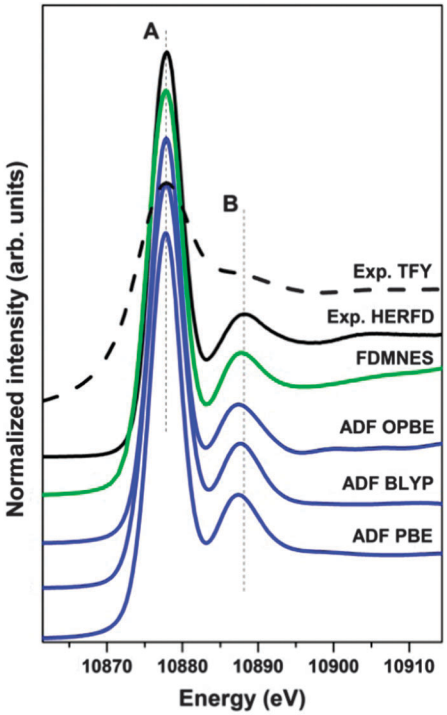

Fig. 3 Experimental and theoretical XANES spectra of Os L_3-edge in $OsCl_3$. Spectra are shifted along the vertical axis for the sake of clarity.

The experimental HERFD and TFY spectra, together with theoretical HERFD spectra of **1** are presented in Fig. 3. Compared to TFY XANES, the high resolution XANES spectrum is much more informative, since the peaks are much sharper. Particularly, peak B is fully resolved and its position and intensity can be assessed unambiguously. The best agreement with the experiment is demonstrated by FDMNES. However, all the spectra simulated with ADF also correspond well to the experiment and are very close to each other. Among them, the energy distance between A and B peaks is most adequately reproduced by the BLYP functional, although all ADF HERFD XANES spectra show somewhat lower absorption in the higher energy region compared to the experimental data.

HERFD and TFY XANES spectra for the complex **2** were measured both in solid state and in acetone solution. The spectra showed similar features, so it is possible to infer that the method is sensitive only to the nearest coordination of the Os atom and that the molecular structure does not experience any significant modifications in this region upon crystallization. Theoretical spectra for **2** were calculated for the three different geometries obtained with different functionals. The results of calculations are presented in Fig. 4 together with the experimental data for the sample in solution. Similarly to the case of osmium trichloride, the HERFD method allows recording considerably sharper spectra. Since the difference in structural parameters obtained by different exchange–correlation functionals is not very large, the difference in the theoretical spectra, calculated by each method is minor as well. The best agreement is achieved for the calculations performed by FDMNES using the

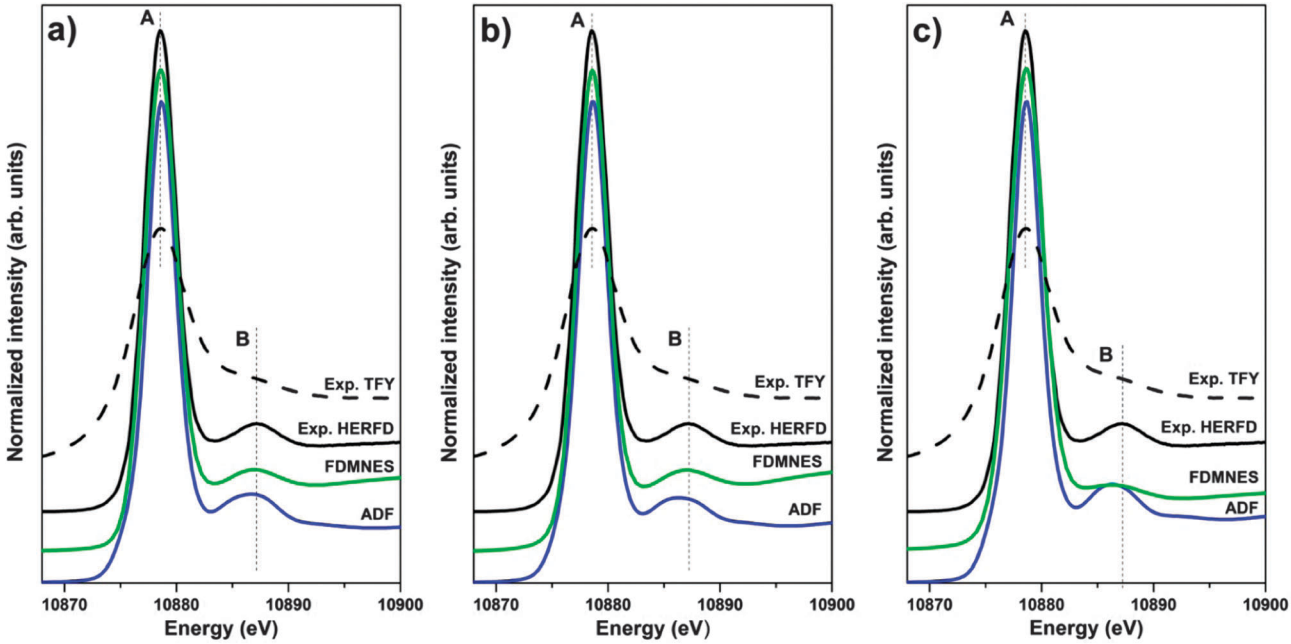

Fig. 4 Experimental and theoretical XANES spectra of the Os L_3-edge in $[Os(bpy)_2(CO)Cl]^+$ calculated for OPBE (a), BLYP (b) and PBE (c) geometries. Spectra are shifted along the vertical axis for the sake of clarity.

geometry computed with BLYP and OPBE functionals. Among the spectra, computed by ADF the best agreement is achieved with the OPBE functional, albeit the shape of peak B is somewhat different from the experimental one. The spectra obtained by ADF using the geometries computed with BLYP and particularly PBE are visibly different from the experiment regarding both relative intensities and energies of the peaks. Quantitative data for the energy splitting of peaks A and B for the two compounds are presented in Table 2, confirming the qualitative observations.

Overall, the specialized FDMNES code allows a better agreement with the experiment to be reached compared to ADF when it is applied for the simulation of L_3-edge HERFD XANES of osmium compounds. However, ADF ground state DFT calculations have the advantage of being less computationally demanding and provide a more precise determination of the Fermi level. FDMNES as well as full multiple scattering codes, such as FEFF,[58] makes a rather rough estimation of the Fermi energy and introduces a parameter, which defines the border between occupied and unoccupied states. Variation of this parameter has a strong influence on the white line intensity and sometimes on its shape. Conversely, the approach based on molecular orbitals does not have this ambiguity since the discrete orbitals have well defined occupations. Moreover, in all-electron calculations, ADF allows analyzing core orbitals, which makes possible the simulation of core-to-core RIXS. The use of a general-purpose DFT code for HERFD XANES computing allows for direct assignment of spectral features. Electronic transitions contributing to the spectrum of **2** together with the most important molecular orbitals calculated with the OPBE functional are presented in Fig. 5. Transitions forming the white line (MOs from 1 to 18) originate mostly from the molecular orbitals situated on the osmium atom and carbonyl or chloride ligands. Bipyridine ligands show almost no contribution, while being the main source of intensity for the second peak (MOs 19–38). Such selectivity creates perspective for using HERFD XANES as a probe for ligand environment of osmium, similarly to X-ray emission spectroscopy[59] and K-pre-edge XANES spectroscopy for 3d transition metals.[60] Spatial distributions of molecular orbitals computed with BLYP functional for **1** are presented in Fig. 6. They suggest that only the absorbing osmium atom and the nearest chlorides contribute to the intensity of the white line while the second peak originates also from the atoms of the second and third coordination spheres.

The influence of the inclusion of a core hole into the calculation of RIXS and XANES is widely discussed in the literature. Kas *et al.* have demonstrated that these effects are of importance

Table 2 Splitting between peaks A and B for experimental and theoretical HERFD XANES spectra of $OsCl_3$ and $[Os(bpy)_2(CO)Cl]^+$

Geometry	Electronic structure	A–B splitting (eV)
	$OsCl_3$	
	Experiment	10.2
OPBE	FDMNES	10.00
OPBE	ADF OPBE	9.60
BLYP	ADF BLYP	9.90
PBE	ADF PBE	9.61
	$[Os(bpy)_2(CO)Cl]^+$	
	Experiment	8.6
OPBE	FDMNES	8.34
OPBE	ADF OPBE	8.04
BLYP	FDMNES	8.42
BLYP	ADF BLYP	7.64
PBE	FDMNES	7.59
PBE	ADF PBE	7.64

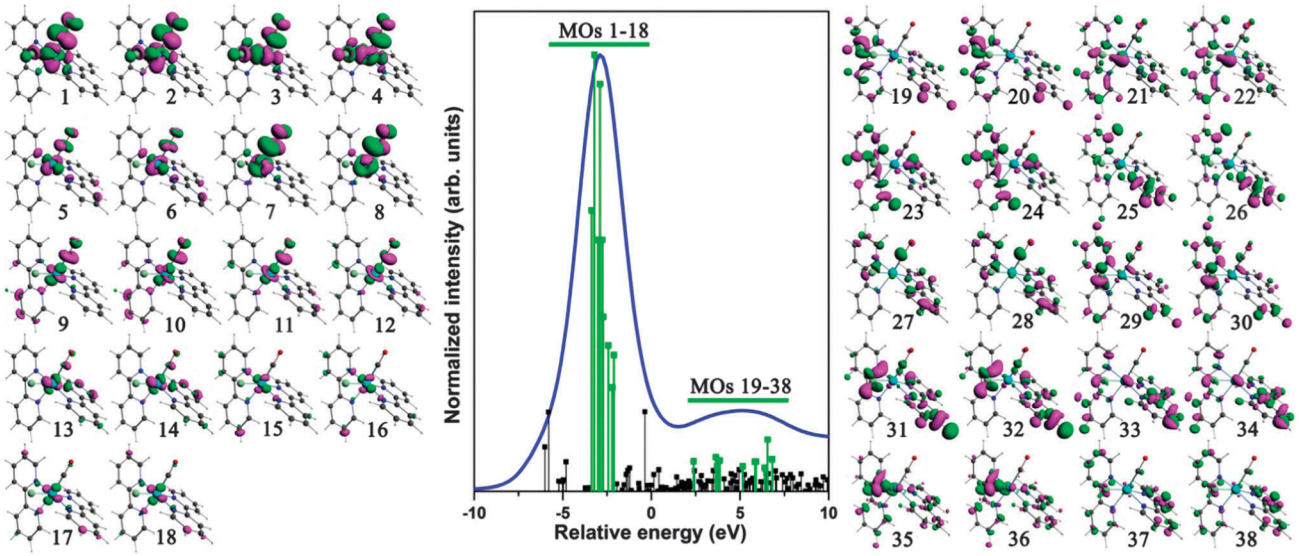

Fig. 5 Electronic transitions contributing to the HERFD XANES spectrum of $[Os(bpy)_2(CO)Cl]^+$. The most intense transitions are highlighted and the spatial distribution of the corresponding molecular orbitals is presented on the left (for the main peak) and on the right (for the second peak) of the graph.

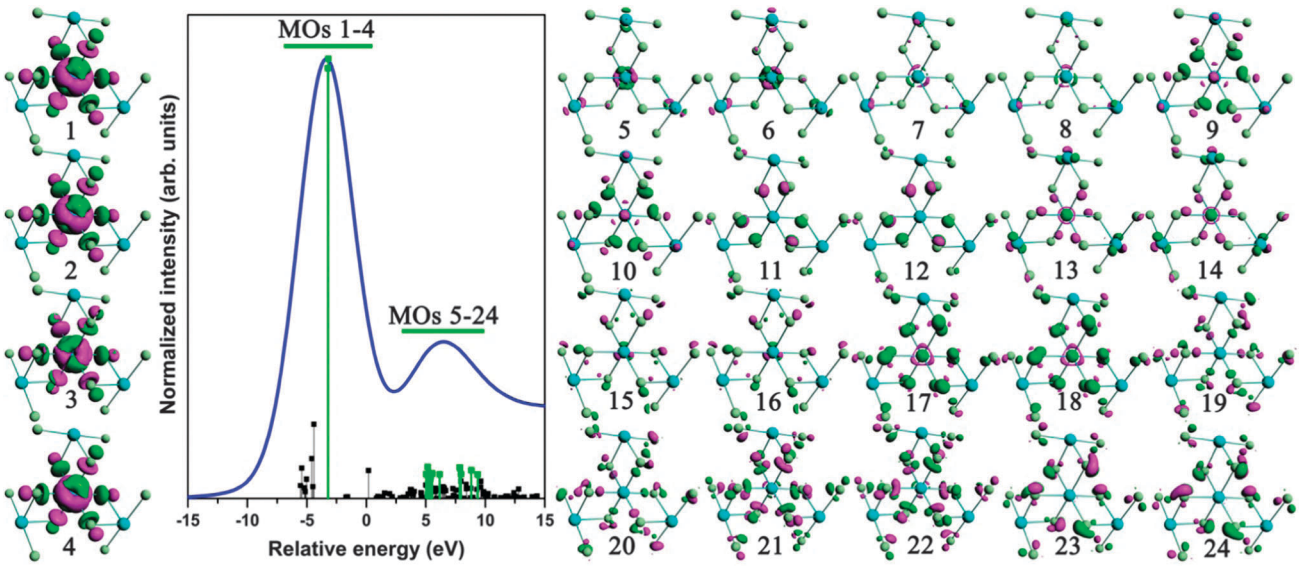

Fig. 6 Electronic transitions contributing to the HERFD XANES spectrum of $OsCl_3$. The most intense transitions are highlighted and the spatial distribution of the corresponding molecular orbitals is presented on the left (for the main peak) and on the right (for the second peak) of the graph.

for Ti Kα, Kβ and $K_{valence}$ RIXS in TiO_2.[61] The FEFF 9 code used in their work allows simulating the core hole using different approaches, such as final state rule and random phase approximation.[62] However, depending on the element and the absorption edge, the strength of core–hole effects may vary. Recently, good results were reported by Alperovich *et al.* for DFT XANES simulations of Ru $L_{2,3}$ edges in various molecular complexes completely neglecting the core–hole.[48,63] Our present results confirm the applicability of ground state DFT calculations with the complete neglect of the core hole for osmium compounds.

First derivatives of the experimental data and theoretical spectra calculated by ADF with a BLYP functional for **1** and OPBE for **2** are presented in Fig. 7. Theoretical spectra are equally scaled and shifted along the energy axis. Analysis of the white line position for the two compounds under study shows that the edge energy of **1** is 1.6 eV lower than the one of **2**, measured as the distance between the inflection points, *i.e.* first derivative maxima. Such shift is opposite to what could be generally expected, since the oxidation state of Os is III in **1** and II in **2**. However, formal oxidation state does not always correspond to the actual charge distribution around the particular atom and, therefore, cannot be unambiguously related to the shift of the absorption edge, as was demonstrated on the example of chromium and manganese K-edges in various compounds.[64,65]

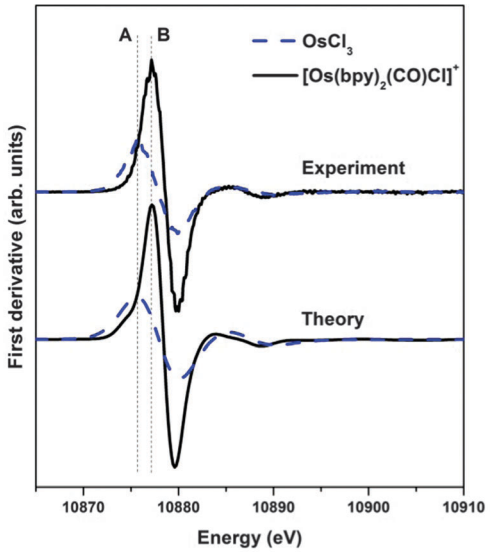

Fig. 7 First derivatives of the experimental and theoretical spectra of $[Os(bpy)_2(CO)Cl]^+$ and $OsCl_3$. Spectra are shifted along the vertical axis for the sake of clarity.

Moreover, the study of iridium complexes by Choy *et al.*[66] shows that L edges may exhibit significant shifts as well within the same formal oxidation state depending on the local environment of the absorbing atom. A similar effect was observed by Glatzel *et al.*[67] in the Pt L_3-edge spectra of potassium chloroplatinates $K_2Pt^{II}Cl_4$ and $K_2Pt^{IV}Cl_6$. In such cases, edges of both conventional TFY and HERFD XANES spectra were strongly redshifted for the compound with higher formal oxidation state of platinum. W and Re $L_{2,3}$ valence-to-core RIXS maps of various oxides reported by Smolentsev *et al.*[1] also suggest that the spectral shape is predominantly determined by the atomic structure. Present results on Os compounds confirm that in this case the edge shifts mainly due to the different ligands and symmetry of the metal site. Therefore, the difference in coordination environment of the osmium atom has more influence on the edge position than the difference in oxidation state.

Conclusions

Large lifetime broadening of Os 2p orbitals makes conventional L-edge XANES spectroscopy hardly suitable for the study of osmium compounds. However, combining X-ray absorption and emission spectroscopy it is possible to reduce the apparent spectral broadening and obtain better resolved spectral features. We have demonstrated here that this approach allows obtaining informative HERFD XANES spectra of Os compounds in both solid and liquid state. Structural models of the studied compounds were refined by the ADF code within DFT formalism. HERFD XANES spectra and RIXS maps were calculated. Specialized XANES code FDMNES and the versatile DFT package ADF both were able to achieve a fair level of agreement with the experiment. Notably, the possibility to obtain good agreement between experiment and DFT simulation results allows employing HERFD XANES and RIXS as quality criteria for the calculated electronic structure which can as well be used to obtain the insight into the origin of various chemical properties of the compounds under study. It was demonstrated that for materials containing heavy atoms such as osmium, the use of advanced RIXS and HERFD XANES spectroscopies makes the extraction of electronic and structural information considerably more reliable compared to the conventional XANES data.

Acknowledgements

LS gratefully acknowledges the MICINN of Spain and the Ramón y Cajal Fellowship RYC-2011-07787. GS acknowledges funding from European Community's Seventh Framework Programme under grant agreement no. 290605 (PSI-FELLOW/COFUND). KL, NS and AS acknowledge the support from the Southern Federal University and the Ministry of Education and Science of the Russian Federation. Authors are grateful to UGINFO computer center of the SFedU for providing the computational time and to Dr. V. N. Datsyuk for technical support.

Notes and references

1 N. Smolentsev, M. Sikora, A. V. Soldatov, K. O. Kvashnina and P. Glatzel, *Phys. Rev. B*, 2011, **84**, 235113.
2 P. Glatzel, J. Singh, K. O. Kvashnina and J. A. van Bokhoven, *J. Am. Chem. Soc.*, 2010, **132**, 2555–2557.
3 C. Garino, E. Gallo, N. Smolentsev, P. Glatzel, R. Gobetto, C. Lamberti, P. J. Sadler and L. Salassa, *Phys. Chem. Chem. Phys.*, 2012, **14**, 15278–15281.
4 F. de Groot and A. Kotani, *Core Level Spectroscopy of Solids*, CRC Press, 2008.
5 P. Glatzel and U. Bergmann, *Coord. Chem. Rev.*, 2005, **249**, 65–95.
6 K. Hämäläinen, D. P. Siddons, J. B. Hastings and L. E. Berman, *Phys. Rev. Lett.*, 1991, **67**, 2850–2853.
7 O. V. Safonova, M. Tromp, J. A. van Bokhoven, F. M. F. de Groot, J. Evans and P. Glatzel, *J. Phys. Chem. B*, 2006, **110**, 16162–16164.
8 S. Bordiga, E. Groppo, G. Agostini, J. A. van Bokhoven and C. Lamberti, *Chem. Rev.*, 2013, **113**, 1736–1850.
9 M. O. Krause and J. H. Oliver, *J. Phys. Chem. Ref. Data*, 1979, **8**, 329–338.
10 Y. Yamashita, Y. Takahashi, H. Haba, S. Enomoto and H. Shimizu, *Geochim. Cosmochim. Acta*, 2007, **71**, 3458–3475.
11 Y. Takahashi, T. Uruga, H. Tanida, Y. Terada, S. Nakai and H. Shimizu, *Anal. Chim. Acta*, 2006, **558**, 332–336.
12 Y. Takahashi, T. Uruga, K. Suzuki, H. Tanida, Y. Terada and K. H. Hattori, *Geochim. Cosmochim. Acta*, 2007, **71**, 5180–5190.
13 N. Sakakibara, Y. Takahashi, K. Okumura, K. T. Hattori, T. Yaita, K. Suzuki and H. Shimizu, *Geochem. J.*, 2005, **39**, 383–389.
14 C. Garino, S. Ghiani, R. Gobetto, C. Nervi, L. Salassa, V. Ancarani, P. Neyroz, L. Franklin, J. B. A. Ross and E. Seibert, *Inorg. Chem.*, 2005, **44**, 3875–3879.
15 Y. Fu, A. Habtemariam, A. M. Pizarro, S. H. van Rijt, D. J. Healey, P. A. Cooper, S. D. Shnyder, G. J. Clarkson and P. J. Sadler, *J. Med. Chem.*, **53**, 8192–8196.

16 L. K. Filak, S. Goschl, S. Hackl, M. A. Jakupec and V. B. Arion, *Inorg. Chim. Acta*, 2012, **393**, 252–260.
17 W. Ginzinger, G. Muhlgassner, V. B. Arion, M. A. Jakupec, A. Roller, M. Galanski, M. Reithofer, W. Berger and B. K. Keppler, *J. Med. Chem.*, 2012, **55**, 3398–3413.
18 K.-L. Wu, S.-T. Ho, C.-C. Chou, Y.-C. Chang, H.-A. Pan, Y. Chi and P.-T. Chou, *Angew. Chem., Int. Ed.*, 2012, **51**, 5642–5646.
19 P. Glatzel, M. Sikora and M. Fernández-García, *Eur. Phys. J. Spec. Top.*, 2009, **169**, 207–214.
20 B. P. Sullivan, J. V. Caspar, T. J. Meyer and S. Johnson, *Organometallics*, 1984, **3**, 1241–1251.
21 G. te Velde and E. J. Baerends, *Phys. Rev. B*, 1991, **44**, 7888–7903.
22 G. Wiesenekker and E. J. Baerends, *J. Phys.: Condens. Matter*, 1991, **3**, 6721.
23 BAND2012, SCM, Theoretical Chemistry, Vrije Universiteit, Amsterdam, The Netherlands, http://www.scm.com.
24 E. van Lenthe and E. J. Baerends, *J. Comput. Chem.*, 2003, **24**, 1142–1156.
25 E. van Lenthe, E. J. Baerends and J. G. Snijders, *J. Chem. Phys.*, 1993, **99**, 4597–4610.
26 E. van Lenthe, E. J. Baerends and J. G. Snijders, *J. Chem. Phys.*, 1994, **101**, 9783–9792.
27 E. van Lenthe, A. Ehlers and E.-J. Baerends, *J. Chem. Phys.*, 1999, **110**, 8943–8953.
28 J. P. Perdew, K. Burke and M. Ernzerhof, *Phys. Rev. Lett.*, 1996, **77**, 3865–3868.
29 G. te Velde, F. M. Bickelhaupt, E. J. Baerends, C. Fonseca Guerra, S. J. A. van Gisbergen, J. G. Snijders and T. Ziegler, *J. Comput. Chem.*, 2001, **22**, 931–967.
30 C. Fonseca Guerra, J. G. Snijders, G. te Velde and E. J. Baerends, *Theor. Chem. Acc.*, 1998, **99**, 391–403.
31 ADF2012, SCM, Theoretical Chemistry, Vrije Universiteit, Amsterdam, The Netherlands, http://www.scm.com.
32 A. D. Becke, *Phys. Rev. A*, 1988, **38**, 3098–3100.
33 C. Lee, W. Yang and R. G. Parr, *Phys. Rev. B*, 1988, **37**, 785–789.
34 N. C. Handy and A. J. Cohen, *Mol. Phys.*, 2001, **99**, 403–412.
35 S. H. Vosko, L. Wilk and M. Nusair, *Can. J. Phys.*, 1980, **58**, 1200–1211.
36 A. D. Becke, *J. Chem. Phys.*, 1993, **98**, 5648–5652.
37 I. Alperovich, A. V. Soldatov, D. Moonshiram and Y. N. Pushkar, *JETP Lett.*, 2012, **95**, 504–510.
38 F. M. F. de Groot, J. C. Fuggle, B. T. Thole and G. A. Sawatzky, *Phys. Rev. B*, 1990, **42**, 5459–5468.
39 E. Stavitski and F. M. F. de Groot, *Micron*, 2010, **41**, 687–694.
40 H. Ikeno, T. Mizoguchi and I. Tanaka, *Phys. Rev. B*, 2011, **83**, 155107.
41 M. W. Haverkort, M. Zwierzycki and O. K. Andersen, *Phys. Rev. B*, 2012, **85**, 165113.
42 P. S. Bagus, H. Freund, H. Kuhlenbeck and E. S. Ilton, *Chem. Phys. Lett.*, 2008, **455**, 331–334.
43 M. Roemelt, D. Maganas, S. Debeer and F. Neese, *J. Chem. Phys.*, 2013, **138**, 204101.
44 M. Roemelt and F. Neese, *J. Phys. Chem. A*, 2013, **117**, 3069–3083.
45 D. Maganas, M. Roemelt, M. Havecker, A. Trunschke, A. Knop-Gericke, R. Schlogl and F. Neese, *Phys. Chem. Chem. Phys.*, 2013, **15**, 7260–7276.
46 F. de Groot, *Coord. Chem. Rev.*, 2005, **249**, 31–63.
47 A. Tougerti, S. Cristol, E. Berrier, V. Briois, C. La Fontaine, F. Villain and Y. Joly, *Phys. Rev. B*, 2012, **85**, 8.
48 I. Alperovich, D. Moonshiram, A. Soldatov and Y. Pushkar, *Solid State Commun.*, 2012, **152**, 1880–1884.
49 Y. Joly, *Phys. Rev. B*, 2001, **63**, 125120.
50 O. Bunău and Y. Joly, *J. Phys.: Condens. Matter*, 2009, **21**, 345501.
51 G. Smolentsev, A. V. Soldatov, J. Messinger, K. Merz, T. Weyhermuller, U. Bergmann, Y. Pushkar, J. Yano, V. K. Yachandra and P. Glatzel, *J. Am. Chem. Soc.*, 2009, **131**, 13161–13167.
52 J. Jiménez-Mier, J. van Ek, D. L. Ederer, T. A. Callcott, J. J. Jia, J. Carlisle, L. Terminello, A. Asfaw and R. C. Perera, *Phys. Rev. B*, 1999, **59**, 2649–2658.
53 H. A. Kramers and W. Heisenberg, *Z. Phys.*, 1925, **31**, 681–708.
54 A. Kotani and S. Shin, *Rev. Mod. Phys.*, 2001, **73**, 203–246.
55 R. Gobetto, C. Nervi, B. Romanin, L. Salassa, M. Milanesio and G. Croce, *Organometallics*, 2003, **22**, 4012–4019.
56 G. Croce, M. Milanesio, D. Viterbo, C. Garino, R. Gobetto, C. Nervi and L. Salassa, *C. R. Chim.*, 2005, **8**, 1676–1683.
57 P. Glatzel, M. Sikora, G. Smolentsev and M. Fernández-García, *Catal. Today*, 2009, **145**, 294–299.
58 J. J. Rehr and R. C. Albers, *Rev. Mod. Phys.*, 2000, **72**, 621–654.
59 K. M. Lancaster, M. Roemelt, P. Ettenhuber, Y. Hu, M. W. Ribbe, F. Neese, U. Bergmann and S. DeBeer, *Science*, 2011, **334**, 974–977.
60 M. Roemelt, M. A. Beckwith, C. Duboc, M.-N. Collomb, F. Neese and S. DeBeer, *Inorg. Chem.*, 2012, **51**, 680–687.
61 J. J. Kas, J. J. Rehr, J. A. Soininen and P. Glatzel, *Phys. Rev. B*, 2011, **83**, 235114.
62 E. L. Shirley, J. A. Soininen and J. J. Rehr, *Phys. Scr.*, 2005, **T115**, 31–34.
63 I. Alperovich, G. Smolentsev, D. Moonshiram, J. W. Jurss, J. J. Concepcion, T. J. Meyer, A. Soldatov and Y. Pushkar, *J. Am. Chem. Soc.*, 2011, **133**, 15786–15794.
64 M. Tromp, J. Moulin, G. Reid and J. Evans, *AIP Conf. Proc.*, 2007, **882**, 699–701.
65 P. Glatzel, G. Smolentsev and G. Bunker, *J. Phys.: Conf. Ser.*, 2009, **190**, 012046.
66 J. H. Choy, S. H. Hwang, J. B. Yoon, C. S. Chin, M. H. Oh and H. G. Lee, *Mater. Lett.*, 1998, **37**, 168–175.
67 P. Glatzel, T.-C. Weng, K. Kvashnina, J. Swarbrick, M. Sikora, E. Gallo, N. Smolentsev and R. A. Mori, *J. Electron Spectrosc. Relat. Phenom.*, 2013, **188**, 17–25.